arXiv:1510.07278v1 [cond-mat.mtrl-sci] 25 Oct 2015

Development of Path Integral Monte Carlo Simulations with Localized Nodal Surfaces for Second-Row Elements

Burkhard Militzer[1,2] and Kevin P. Driver[1]

[1]*Department of Earth and Planetary Science, University of California, Berkeley*
[2]*Department of Astronomy, University of California, Berkeley*

We extend the applicability range of fermionic path integral Monte Carlo simulations to heavier elements and lower temperatures by introducing various localized nodal surfaces. Hartree-Fock nodes yield the most accurate prediction for pressure and internal energy that we combine with the results from density functional molecular dynamics simulations to obtain a consistent equation of state for hot, dense silicon under plasma conditions and in the regime of warm dense matter (2.3−18.6 g cm^{-3}, $5.0 \times 10^5 - 1.3 \times 10^8$ K). The shock Hugoniot curve is derived and the structure of the fluid is characterized with various pair correlation functions.

PACS numbers: 62.50.-p,31.15.A-,61.20.Ja,64.30.-t

The development of a first-principles methodology for warm dense matter (WDM) applications that treats temperature effects consistently is a key component of the stewardship of plasma science [1, 2]. Indeed, technological progress in high energy density physics (HEDP) applications, such as fusion energy [3, 4], shock-wave physics [5], astrophysical processes [6–8], and planetary [9, 10] and stellar [11] interiors, relies on simulations for input and guidance. WDM is broadly described as the HEDP regime between condensed matter and ideal plasmas, where strong electron correlation and quantum and ionization effects are all important.

For the low temperature part of the WDM regime, density functional molecular dynamics (DFT-MD) [12] is an accurate and efficient first-principles simulation method. The thermal occupation of electronic states is treated as a perturbation of the ground state by Fermi-Dirac smearing [13]. The main drawback of this method is that it becomes computationally infeasible as electrons occupy more bands with increasing temperature. Some alternative DFT-MD-based methods, such as orbital-free DFT [14, 15] and average-atom models [16], have made progress on overcoming the thermal-occupation deficiency, but efforts to improve accuracy are still underway [17, 18].

Here, we focus on the development of the path integral Monte Carlo (PIMC) method [19], which naturally incorporates finite temperature quantum effects by working within the many-body thermal density matrix formalism. The combination with Monte Carlo sampling makes this approach one of the most appropriate first-principles simulation techniques for quantum systems at finite temperature, (T). Since the length of the path scales like $1/T$, the method becomes increasingly efficient for high temperatures. Electrons and nuclei are often treated equally as paths but here we treat the nuclei classically because their zero-point motion is negligible for the temperatures under consideration.

PIMC simulations with more than two electrons in a dense system suffer from a fermion sign problem, which we solve by introducing the the fixed node approximation [20, 21] that restricts paths to remain in the positive regions of a trial density matrix, $\rho_T(\mathbf{R}, \mathbf{R}_t; t) > 0$. The restricted path integral reads,

$$\rho_F(\mathbf{R}, \mathbf{R}'; \beta) = \frac{1}{N!} \sum_{\mathcal{P}} (-1)^{\mathcal{P}} \int_{\mathbf{R} \to \mathcal{P}\mathbf{R}',\, \rho_T > 0} \mathbf{dR}_t \;\; e^{-S[\mathbf{R}_t]}, \quad (1)$$

where the action, S, weights every path and $\mathcal{P}$ denotes permutations of identical particles. The most common approximation to the trial density matrix is a Slater determinant of single particle density matrices,

$$\rho_T(\mathbf{R}, \mathbf{R}'; \beta) = \left|\left| \rho^{[1]}(r_i, r'_j; \beta) \right|\right|_{ij} , \quad (2)$$

in combination with the free particle (FP) density matrix,

$$\rho_0^{[1]}(r, r'; \beta) = \sum_k e^{-\beta E_k} \, \Psi_k(r) \, \Psi_k^*(r') \quad , \quad (3)$$

derived from a sum over plane waves, $\Psi_k(r)$. The latter is usually converted into Gaussian form [20]. FP nodes becomes exact in the limit of high temperature. Interaction effects have been introduced to the nodal structure on the variational level [22, 23].

In previous work [24–29], we have shown FP nodes can be sufficient to bridge the WDM regime for elements as heavy as neon. FP nodes work for first-row elements because they can still describe the occupation of the 1s state and DFT-MD works well for lower temperatures where the second shell becomes occupied. In order to simulate second-row elements with PIMC, one must go beyond the FP nodal approximation and incorporate the effects of bound states as we describe below in an application to silicon.

We chose to study silicon since it is a natural extension of our original work on carbon and a prototype material with relevance in the semiconductor industry [30], geophysics and planetary science [10], and astrophysics [11, 31–35]. Silicon has a rich solid phase diagram, displaying 11 solid-state phases under pressure, becoming metallic near 12 GPa [36–38]. A number of dynamic shock compression experiments have been performed [39–45]. Shock-compressed silicon has been studied theoretically with several classical [46–49] and one DFT-MD simulation [50] that investigated pressures up

to 500 GPa and temperatures up to 10^4 K. Dynamical properties of shocked silicon plasma states have also been studied extensively by theoretical approaches [51–55].

We perform standard DFT-MD simulations using the VASP code [56]. Exchange-correlation effects are described using the Perdew-Burke-Ernzerhof [57] functional, which was not explicitly designed for finite temperature [58], but previous PIMC and DFT-MD work [24, 26, 27, 29], has shown this approximation is reliable. We use a plane-wave energy cut-off of up 4000 eV and a small-core ($r_{\rm core}$=1.0 Å), PAW [59] pseudopotential with 12 valence electrons. We used up to 9000 bands to converge the thermal occupation to better than 10^{-4}. All simulations are performed at the Γ-point of the Brillouin zone, which is sufficient for high temperature fluids.

Supercells with 8 atoms were used for $T \geq 2.5 \times 10^5$ K where the kinetic energy far outweighs the interaction energy, and 24-atoms were used at lower temperatures [29]. Additional details are provided in the appendix. For the PIMC calculations, we have used our own code CUPID [60]. The Coulomb interaction is introduced through pair density matrices [61–63]. The nodes are enforced at intervals of 1/8192 Ha, which means we need between 4 and 2560 time slices for simulations in the temperature range of $129 - 1 \times 10^6$ K. It is sufficient to evaluate the pair action only at intervals of 1/1024 Ha [23].

We began our investigation of localized nodal approximations in PIMC with the relatively simple, proof-of-concept problem of computing internal energy and pressure of a stationary silicon atom (one nucleus and 14 electrons) in a periodic cell over a wide temperature range. In Fig. S1, we compared energies from DFT and PIMC using FP nodes, where we found a discrepancy of 5.2 Ha/atom already at 2×10^6 K that increased to 12.6 Ha at 5×10^5 K. We attributed this discrepancy primarily to the FP nodal approximation, which we have shown to work well only as long as the second shell is not significantly occupied [27].

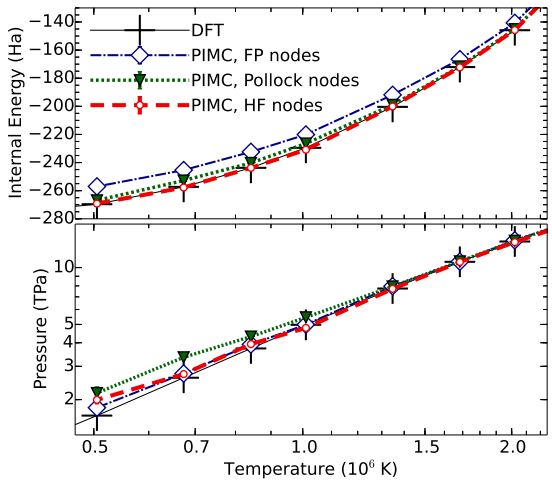

FIG. 1: Internal energy and pressure vs. temperature for a single silicon atom in periodic cell of 5.0 Bohr.

We investigated two approaches to improve upon the FP nodal approximation. First, we added the bound eigenstates of the Coulomb potential of the silicon nuclei, $\Psi_s(r - R_I)$, to the nodal approximation in Eq. 3:

$$\rho^{[1]}(r, r', \beta) = \sum_{I=1}^{N} \sum_{s=0}^{n} e^{-\beta E_s} \Psi_s(r - R_I) \Psi_s^*(r' - R_I) \ , \quad (4)$$

where the number of states, n, needs to be at least 7 in each spin channel in order to provide at least one bound state for every electron. We used the efficient formulation of the Coulomb density matrix put forth in Ref. [61] and hence refer to this approximation as Pollock nodes. The 1s state ($n = 1$) has been added to PIMC nodes once before to simulate dense hydrogen [64]. However agreement with DFT predictions and experimental results was not as good as expected because additional approximations were introduced when the nodes were enforced. Here we enforce the nodes strictly as outlined in Refs. [20, 21].

The adoption of Pollock nodes reduced the energy deviation between DFT and PIMC from 12.6 to 2.7 Ha at 5×10^5 K. However, the pressure deviations increased from 11 to 31% (Fig. S1). We tried to improve upon this result by varying the number of bound states in Eq. 4, testing different time steps, studying various numbers of electrons, and finally by developing a multi-determinental nodal surface in the spirit of quantum chemistry. In the multi-determinantal approach, we adopted a sum of FP fermion determinants where each is added to a different bound shell with the appropriate $e^{-\beta E_s}$ weight. However, this approach did not lead to a significant improvement in the predicted pressure. This discrepancy led us to abandon the Pollock node approximation. We concluded that the eigenstates of noninteracting particles in the Coulomb potential are too confining for interacting electrons.

In our second approach, we constructed a thermal density matrix from Hartree-Fock (HF) orbitals that we computed with the GAMESS code [65] and expanded in a localized basis set (6-31++G). We use again Eq. 4 but this time the functions $\Psi_s(r)$ become the HF orbitals, which are weighted by factors $e^{-\beta E_s}$ where E_s is set to the corresponding HF eigenvalues. Our approach differs from groundstate HF nodes [66]. With our HF nodal approximation, we found perfect agreement with the DFT prediction for the internal energy of the silicon atom over the entire temperature range under consideration (Fig. S1). The resulting PIMC energies are consistently lower than those obtained with other two nodal approximations, which, as illustrate in the appendix, implies a lower free energy [23] and establishes HF nodes as the most accurate nodes among the three approximations considered here. The PIMC pressures derived with HF nodes agree within the 1 σ error bars for all temperatures of 7×10^5 K and higher. For 5×10^5 K, a small pressure discrepancy remained, but, given the large improvement over FP and Pollock nodes, we decide to adopt HF nodes for our many-particle simulations with moving nuclei that we discuss for the remainder of this article.

The evaluation of HF orbitals for many moving particles adds a non-negligible burden to computation of the nodes. We vectorized this part of the calculation by evaluating the orbitals for many positions at once. We update the inverse of the determinants whenever possible rather than recomputing it. Nevertheless, when one ion is moved, all determinants need to be re-evaluated, which is not the case for FP nodes that are independent of the ion positions. Despite this additional cost, we were able to perform PIMC simulations with 8 nuclei and 112 electrons for temperatures of 1×10^6 K and above.

We needed to introduce one more methodological development. Upon introducing HF nodes into our simulations with moving nuclei, the acceptance ratio for ion moves rapidly decayed to zero at lower and intermediate temperatures as electron paths began to sample the bound states at the nuclei. Because the nodal surfaces now depend on the nuclear positions, node crossings are almost unavoidable when an ion is moved. The crossing is almost exclusively triggered by nearby electrons. The decay in efficiency was so detrimental that we could not have obtained the smooth $g(r)$ functions in Fig. 2 without the development of multi-particle moves that relocate one nucleus and nearby electrons at once. We needed to design an algorithm that satisfies the detailed balance requirement [19] and does not rely on any permanent pairing of electrons and ions. We introduced a localization function,

$$L_{Ij} = \int_0^\beta dt \; |\Psi_{1s}(r_j(t) - R_I)|^2 \;, \qquad (5)$$

that assigns a probability of finding electron paths, $r_j(t)$, near ion, I. Adopting concepts from the permutation sampling in Ref. [19], we multiply these probabilities to construct a table that contains all moves of one ion with up to four electron paths including those that permute. Because L_{Ij} is a very localized function, the number of significant entries is fairly small so that the table can be constructed efficiently. Once a particular move has be selected from the table, we shift the entire group to a new location within a box of 0.5 Bohr without otherwise changing their paths. This leaves the function L_{Ij} unchanged within the group, which means detailed balance can be satisfied by adopting a particularly simple expression for the acceptance ratio: the sum of table entries for the new location divided by that for the original coordinates. This procedure led to very efficient ion moves. To change internal coordinates of electron paths, we keep relying the on single and multi-electron moves [19].

Figure 3 and Tab. summarize our equation of state calculations. For density interval of 1 to 8-fold the ambient density of 2.329 g cm^{-3}, PIMC simulations with HF nodes were performed for a temperature range of $129 - 2 \times 10^6$ K and DFT-MD simulations for $2 - 0.05 \times 10^6$ K. At 2×10^6 K, both methods yield consistent thermodynamic and structural properties despite the fact that both techniques involve very different concepts and approximations. The predicted internal energies deviate by up to 5 Ha/atom and the pressure by up to 4%. A difference of 5 Ha/atom would be equivalent to a

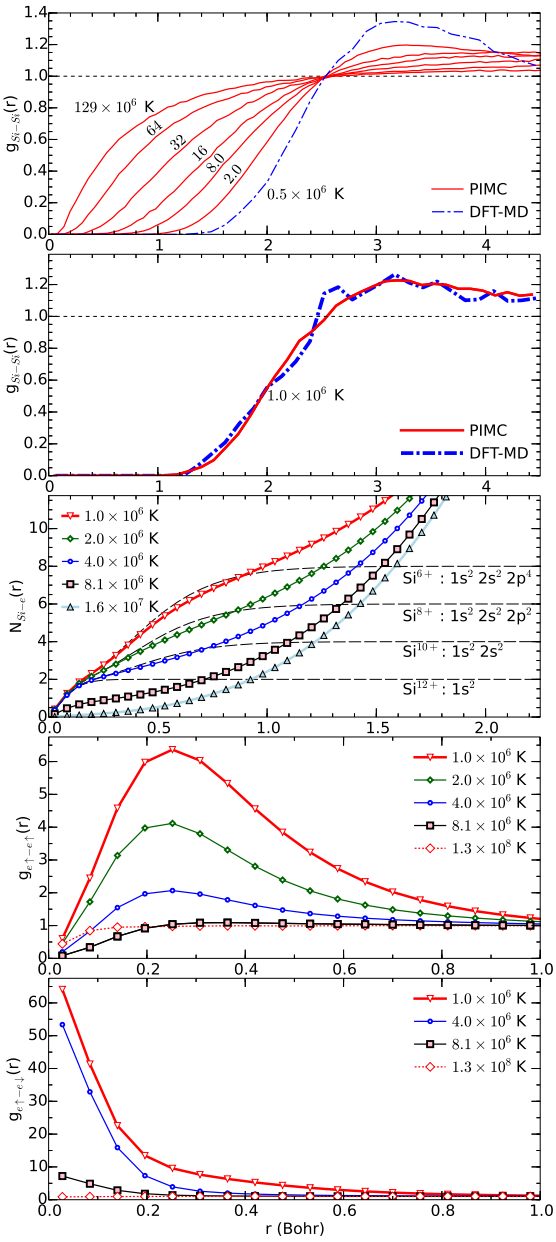

FIG. 2: The top two panels compare the nuclear pair correlation functions from PIMC and DFT-MD at various temperatures. The middle panel shows the integrated nucleus-electron pair correlation function, $N(r)$, computed with PIMC. Results are compared with an isolated ion in order to estimate the ionization state of the plasma. The two lowest panels display the electron-electron pair correlation functions for pairs with parallel and opposite spins. All results are for 4-fold compression.

2.5% difference in the ionization fraction of the second shell. We attribute these deviations to a combined effect of three approximations: the groundstate DFT exchange-correlation functional, the frozen-core DFT pseudopotential, and our localized nodes in PIMC. While it is difficult to disentangle the errors due to these approximations, we anticipate that the discrepancies will be reduced further when both methods are im-

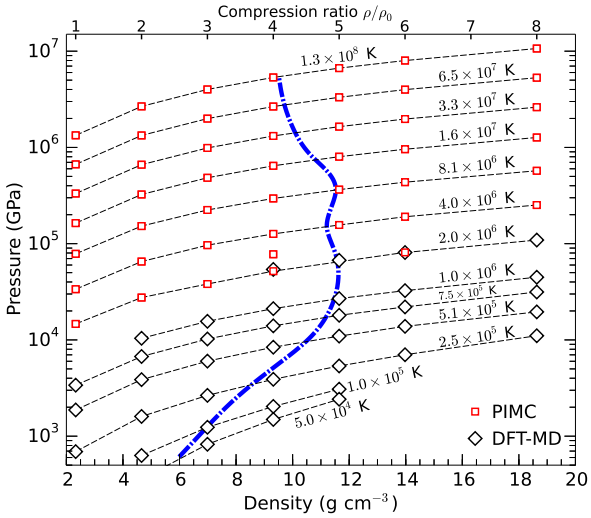

FIG. 3: Pressure-density conditions of our PIMC and DFT-MD simulations. The blue line shows the shock Hugoniot curve.

proved in the future. Figure 4 illustrates that the deviations between PIMC and DFT-MD are small compared to the error in the Debye model. We only plotted excess quantities relative to a fully ionized plasma model because the total internal energy varies by over 10 000 Ha/atom in the parameter range of consideration.

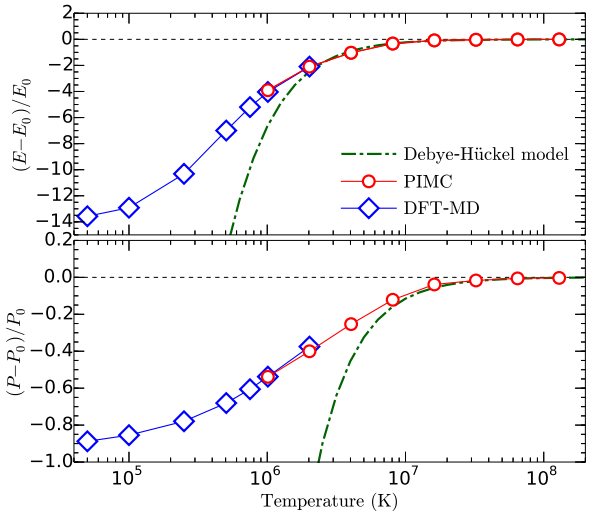

FIG. 4: Internal energy and pressure for a silicon plasma at a density of 9.316 g cm^{-3} are shown versus temperature. We plot the excess quantities relative to a fully ionized noninteracting plasma.

Good agreement between PIMC and DFT-MD is found for the nuclear pair correlation shown in Fig. 2. With PIMC we were also able to derive the integrated nucleus-electron pair correlation function, $N(r)$, that measures how many electron reside on average within a radius, r, from a nucleus. Comparing the information at small r with results for isolated ions, we can estimate the degree of ionization in the plasma. For temperatures of 1, 2, and 4 $\times 10^6$ K, we estimate the average charge of the silicon ions to be +6, +8, and +10 respectively. At higher temperature the 1s states becomes partially ionized also.

The electron-electron pair correlation functions in Fig. 2 yield strong positive correlations, which underlines that multiple electrons are bound to one nucleus. As the temperature is increased, the positive correlation diminishes and eventually even the negative correlations between electrons with parallel spins at small r is reduced.

Finally we derive the principal shock Hugoniot [67]. Under shock compression, a material changes from a initial state with internal energy, pressure, and volume ($E_0 = -289.166$ Ha/atom, P_0=1 bar, V_0 from $\rho_0 = 2.329$ g cm^{-3}) to a final state denoted by (E, P, V) that we can predict theoretically. The shock compression ratio, ρ/ρ_0, is controlled by interaction effects and by excitations of internal degrees of freedom. In Fig. 3, a maximum compression ratio of 4.99 is reached for 1.6×10^6 K where approximately 7 of 14 electrons have been ionized. A second compression maximum of 4.95 is predicted to occur at 8.3×10^6 K, which is caused by the ionization of the 1s state. As we have seen for neon [29], the temperature is too high for this maximum to be studied with DFT-MD. Therefore a combined PIMC and DFT-MD approach is needed to study all features of the principal Hugoniot curve.

By constructing a thermal density matrix with HF orbitals for the purpose of computing fermion nodes, we were able to perform PIMC simulations with heavier elements than was possible before. Through the optimized evaluation of such nodes and the adoption of multi-particle Monte Carlo moves we were able to put together an efficient algorithm and derive the equation of state of silicon plasmas. At lower temperature, we add results from standard DFT-MD simulations. By combining both techniques, we provide a first-principles treatment for all second-row elements in the regime of warm dense matter and for plasma conditions.

This research is supported by the U.S. Department of Energy, Grant No. de-sc0010517. Computational support was provided by NASA, NERSC, and NCAR. B. Austin provided support for reading in the Gamess orbitals. J. Demmel gave advice on the numerics of determinant evaluations.

[1] R. Betti, editor. *Advancing the Science of High Energy Density Laboratory Plasmas*, Washington D.C., 2009. Office of Fusion Energy Science (OFES)/Fusion Energy Science Advisory Committee (FESAC).

[2] R. Rosner, D. Hammer, and T. Rothman, editors. *Basic Research Needs for high energy density laboratory physics*, Washington D.C., 2009. U.S. Department of Energy.

[3] M. Keith Matzen, M. A. Sweeney, R. G. Adams, J. R. Asay, J. E. Bailey, G. R. Bennett, D. E. Bliss, D. D. Bloomquist, T. A. Brunner, R. B. Campbell, G. A. Chandler, C. A. Coverdale, M. E. Cuneo, J.-P. Davis, C. Deeney, M. P. Desjarlais, G. L. Donovan, C. J. Garasi, T. A. Haill, C. A. Hall, D. L. Hanson, M. J. Hurst, B. Jones, M. D. Knudson, R. J. Leeper, R. W.

Lemk̃e, M. G. Mazarakis, D. H. McDaniel, T. A. Mehlhorn, T. J. Nash, C. L. Olson, J.L̃. Porter, P. K. Rambo, S. E. Rosenthal, G. A. Rochau, L. E. Ruggles, C. L. Ruiz, J. F. Sanford, T. W. L. a nd Seamen, D. B. Sinars, S. A. Slutz, I. C. Smith, K. W. Struve, W. A. Stygar, R.Ã. Vesey, E. A. Weinbrecht, D. F. Wenger, and E. P. Yu. Pulsed-power-driven high energy density physics and inertial confinement fusion research. *Phys. Plasmas*, 12:055503, 2005.

[4] I. Cook. Materials research for fusion energy. *Nat. Mater.*, 5:77, 2006.

[5] R. Cauble, D. K. Bradley, P. M. Celliers, G. W. Collins, L. B. Da Siliva, and S. J. Moon. Experiments Using Laserdriven Shockwaves for EOS and Transport Measurements. *Contrib. Plasma Physics*, 41:239, 2001.

[6] H. M. Van Horn. Dense astrophysical plasmas. *Science*, 252:384, 1991.

[7] G. Chabrier, F. Douchin, and A. Y. Potekhin. Dense astrophysical plasmas. *J. Phys.: Condens. Matter*, 14:9133, 2002.

[8] M. Cotelo, P. Velarde adn A. G. de la Varga, and C. Garcia-Fernandez. *Astrophys. Space Sci.*, 336:53, 2011.

[9] J. J. Fortney, S. H. Glenzer, M. Koenig, B. Militzer, D. Saumon, and D. Valencia. Frontiers of the physics of dense plasmas and planetary interiors: Experiments, theory, and applications. *Phys. Plasmas*, 16:041003, 2009.

[10] A. Bennuzzi-Mounaix, S. Mazevet, A. Ravasio, T. Vinci, A. Denoeud, M. Koenig, N. Amadou, E. Brambrink, F. Festa, A. Levy, M. Harmand, S. Brygoo, G. Huser, V. Recoules, J. Bouchet, G. Morard, F. Guyot, T. de Resseguier, K. Myanishi, N. Ozaki, F. Dorchies, J. Gaudin, P. M. Leguay, O. Peyrusse, O. Henry, D. Raffestin, S. Le Pape, R. Smith, and R. Musella. Progress in warm dense matter study with applications to planetology. *Phys. Scr.*, T161:014060, 2014.

[11] C.J. Hansen and S.D. Kawaler. *Stellar Interiors: Physical Principles, Structure, and Evolution*, volume 1 of *Astronomy and astrophysics library*. Springer-Verlag New York, 1994.

[12] Dominik Marx and Jurg Hutter. Ab initio molecular dynamics: Theory and implementation. *Modern methods and algorithms of quantum chemistry*, 1:301–449, 2000.

[13] M. Verstraete and X. Gonze. *Phys. Rev. B*, 65, 2001.

[14] F. Lambert and J. Clérouin and S. Mazevet. Structural and dynamical properties of hot dense matter by a Thomas-Fermi-Dirac molecular dynamics. *Europhys. Lett.*, 75:681, 2006.

[15] F. Lambert, J. Clérouin, S. Mazevet, and D. Gilles. Properties of hot dense plasmas by orbital-free molecular dynamics. *Contrib. Plasma Phys.*, 47:272–280, 2007.

[16] B. F. Rozsnyai. Equation of state calculations based on the self-consistent ion-sphere and ion-correlation average atom models. *High. Energy Dens. Phys.*, 16, 2014.

[17] V. V. Karasiev, D. Chakraborty, O. A. Shukruto, and S. B. Trickey. *Phys. Rev. B*, 88, 2013.

[18] T. Sjostrom and J. Daligault. *Phys. Rev. Lett.*, 113, 2014.

[19] D. M. Ceperley. *Rev. Mod. Phys.*, 67:279, 1995.

[20] D. M. Ceperley. *J. Stat. Phys.*, 63:1237, 1991.

[21] D. M. Ceperley. In Ed. K. Binder and G. Ciccotti, editors, *Monte Carlo and Molecular Dynamics of Condensed Matter Systems*. Editrice Compositori, Bologna, Italy, 1996.

[22] B. Militzer and E. L. Pollock. *Phys. Rev. E*, 61:3470, 2000.

[23] B. Militzer and D. M. Ceperley. *Phys. Rev. Lett.*, 85:1890, 2000.

[24] B. Militzer, D. M. Ceperley, J. D. Kress, J. D. Johnson, L. A. Collins, and S. Mazevet. *Phys. Rev. Lett.*, 87:275502, 2001.

[25] B. Militzer. *Phys. Rev. Lett.*, 97:175501, 2006.

[26] B. Militzer. *Phys. Rev. B*, 79:155105, 2009.

[27] K. P. Driver and B. Militzer. All-electron Path Integral Monte Carlo Simulations of Warm Dense Matter: Application to Water and Carbon Plasmas. *Phys. Rev. Lett.*, 108:115502, 2012.

[28] L. X. Benedict, K. P. Driver, S. Hamel, B. Militzer, T. Qi, A. A. Correa, A. Saul, and E. Schwegler. A multiphase equation of state for carbon addressing high pressures and temperatures. *Phys. Rev. B*, 89:224109, 2014.

[29] K. P. Driver and B. Militzer. First-principles simulations and shock Hugoniot calculations of warm dense neon. *Phys. Rev. B*, 91:045103, 2015.

[30] J. Liu and J. Cao and S. Kaierle, editor. *Deformation behavior of single crystal silicon induced by laser shock peening*, volume 8796. American Institute of Physics, 2013.

[31] E. Herbst, Tj Millar, S. Wlodek, and Dk Bohme. The chemistry of silicon in dense interstellar clouds. *Astron. Astrophys.*, 222:205, 1989.

[32] William D. Langer and a. E. Glassgold. Silicon chemistry in interstellar clouds. *Astrophys. J.*, 352:123, 1990.

[33] D. D. S. MacKay. *Mon. Not. R. Astron. Soc.*, 274:694, 1995.

[34] P Schilke, C.˜M. Walmsley, G Pineau des Forets, and D.˜R. Flower. SiO production in interstellar shocks. *Astron. Astrophys.*, 321:293, 1997.

[35] A. P. Jones, A. G. G. M. Tielens, D. J. Hollenbach, and C. F. Mckee. Grain destruction in shocks in the interstellar medium. *Astrophys. J.*, 433:797, 1994.

[36] A. Mujica and A. Rubio and A. Muñoz. High-pressure phases of group-IV , III V , and II VI compounds. *Rev. Mod. Phys.*, 75:863, 2003.

[37] D. Alfè, M. J. Gillan, M. D. Towler, and R. J. Needs. Diamond and β-tin structures of Si studied with quantum Monte Carlo calculations. *Phys. Rev. B*, 70:214102, 2004.

[38] R. G. Hennig, A. Wadehra, K. P. Driver, W. D. Parker, C. J. Umrigar, and J. W. Wilkins. Phase transformation in Si from semiconducting diamond to metallic beta-Sn phase in QMC and DFT under hydrostatic and anisotropic stress. *Phys. Rev. B*, 82:014101, 2010.

[39] P. Celliers, a. Ng, G. Xu, and a. Forsman. Thermal equilibration in a shock wave. *Phys. Rev. Lett.*, 68:2305, 1992.

[40] R. R. Alcon and D. L. Robbins and S. A. Sheffield and D. B. Stahl and J. N. Fritz. Shock Compression of Silicon Polymer Foams with a Range of Initial Densities. *AIP Conf. Proc.*, 706:651, 1977.

[41] Sd Gilev and Am Trubachev. Metallization of Monocrystalline Silicon under Shock Compression. *Phys. Status Solidi B Basic Res.*, 211:379, 1999.

[42] S D Gilev and a M Trubachev. Metallization of silicon in a shock wave: the metallization threshold and ultrahigh defect densities. *J. Phys. Condens. Matter*, 16(46):8139, 2004.

[43] Th. Löwer, V. Kondrashov, M. Basko, a. Kendl, J. Meyer-ter Vehn, R. Sigel, and a. Ng. Reflectivity and Optical Brightness of Laser-Induced Shocks in Silicon. *Phys. Rev. Lett.*, 80:4000, 1998.

[44] a. Loveridge-Smith, a. Allen, J. Belak, T. Boehly, a. Hauer, B. Holian, D. Kalantar, G. Kyrala, R. W. Lee, P. Lomdahl, M. a. Meyers, D. Paisley, S. Pollaine, B. Remington, D. C. Swift, S. Weber, and J. S. Wark. Anomalous elastic response of silicon to uniaxial shock compression on nanosecond time scales. *Phys. Rev. Lett.*, 86:2349, 2001.

[45] H Kishimura, H Matsumoto, and N N Thadhani. Effect of shock compression on single crystalline silicon. *J. Phys. Conf. Ser.*, 215:012145, 2010.

[46] Gabriele Mogni, Andrew Higginbotham, Katalin Gaál-Nagy, Nigel Park, and Justin S. Wark. Molecular dynamics simulations of shock-compressed single-crystal silicon. *Phys. Rev. B*, 89:064104, 2014.

[47] Evan J. Reed. Hugoniot Constraint Molecular Dynamics Study

of a Transformation to a Metastable Phase in Shocked Silicon. *AIP Conf. Proc.*, 620:343, 2002.
[48] Zhongyu Li, Di Chen, Jing Wang, and Lin Shao. Molecular dynamics simulation of Coulomb explosion, melting and shock wave creation in silicon after an ionization pulse. *J. Appl. Phys.*, 115:143507, 2014.
[49] I. I. Oleynik, S. V. Zybin, M. L. Elert, and C. T. White. Nanoscale molecular dynamics simulaton of shock compression of silicon. *AIP Conf. Proc.*, 845(2006):413, 2006.
[50] D. Swift, G. Ackland, a. Hauer, and G. Kyrala. First-principles equations of state for simulations of shock waves in silicon. *Phys. Rev. B*, 64:214107, 2001.
[51] A. Ng, P. Celliers, G. Xu, and A. Forsman. Electron-ion equilibration in a strongly coupled plasma. *Phys. Rev. E*, 52:4299, 1995.
[52] M. D. Furnish, N. N. Thadhani, and Y. Horie, editors. *Shock Waves and Plasma Physics*. American Institute of Physics, 2002.
[53] A. Ng. *International Journal of Quantum Chemistry*, 112:150, 2011.
[54] J. Vorberger, D. O. Gericke, Th Bornath, and M. Schlanges. Energy relaxation in dense, strongly coupled two-temperature plasmas. *Phys. Rev. E*, 81:046404, 2010.
[55] J. Vorberger, Z. Donko, I. M. Tkachenko, and D. O. Gericke. Dynamic ion structure factor of warm dense matter. *Phys. Rev. Lett.*, 109:225001, 2012.
[56] G. Kresse and J. Furthmüller. Efficient iterative schemes for ab initio total-energy calculations using a plane-wave basis set. *Phys. Rev. B*, 54:11169, 1996.
[57] J. P. Perdew, K. Burke, and M. Ernzerhof. Generalized gradient approximation made simple. *Phys. Rev. Lett.*, 77:3865, 1996.
[58] E. W. Brown, B. K. Clark, J. L. DuBois, and D. M. Ceperley. Path-Integral Monte Carlo Simulations of the Warm Dense Homogeneous Electron Gas. *Phys. Rev. Lett.*, 110:146405, 2013.
[59] P. E. Blöchl. Projector augmented-wave method. *Phys. Rev. B*, 50:17953, 1994.
[60] B. Militzer. PhD thesis, University of Illinois at Urbana-Champaign, 2000.
[61] E. L. Pollock. *Comp. Phys. Comm.*, 52 :49, 1988.
[62] V. Natoli and D. M. Ceperley. *J. Comp. Phys.*, 117:171–178, 1995.
[63] B. Militzer and R. L. Graham. *Journal of Physics and Chemistry of Solids*, 67:2136, 2006.
[64] S. A. Khairallah and J. Shumway and E. Draeger, available on arXiv:1108.1711.
[65] M.W.Schmidt, K.K.Baldridge, J.A.Boatz, S.T.Elbert, M.S.Gordon, J.J.Jensen, S.Koseki, N.Matsunaga, K.A.Nguyen, S.Su, T.L.Windus, M.Dupuis, and J.A.Montgomery. *J. Comput. Chem.*, 14:1347, 1993.
[66] J. Shumway. All-Electron Path Integral Monte Carlo Simulations of Small Atoms and Molecules. In *Computer Simulation Studies in Condensed-Matter Physics XVI*, page 181. Springer Berlin Heidelberg, 2006.
[67] Y. B. Zeldovich and Y. P. Raizer. *Elements of Gasdynamics and the Classical Theory of Shock Waves*. Academic Press, New York, 1968.

Appendix: Internal Energy Comparison for Different Nodal Surface

In Fig. S1, we plot the internal energy difference between PIMC calculations with various nodal surfaces for the isolated silicon atom that we already reported in a alternate format in figure 1 of the article. For this specific example, one finds that FP particle nodes are sufficiently accurate for $T \geq 4.0 \times 10^6$ K. For $T \geq 1.7 \times 10^6$ K, PIMC results obtained with Pollock nodes agree reasonably well with predictions from HF nodes, our most reliable nodal approximation.

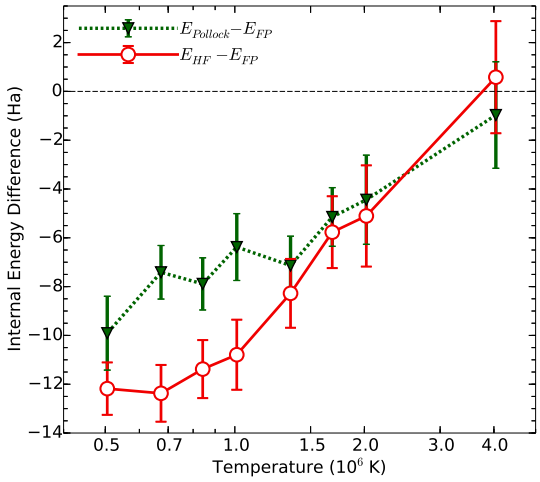

FIG. S1: Difference in internal energy between PIMC calculations using Pollock, Hartree-Fock (HF), and free-particle (FP) nodes for a single silicon atom in periodic cell of 5.0 Bohr.

The internal energies, E, obtained with HF nodes are consistently lower than those with both other nodal surfaces. Therefore, the HF nodes are our most accurate nodal surface because they lead to the lowest free energy, F. In fermionic PIMC, the best nodal surface can be established by minimizing the free energy [23]. F is given by the integral over the internal energy, E,

$$\beta_2 F(\beta_2, V) = \beta_1 F(\beta_1, V) + \int_{\beta_1}^{\beta_2} d\beta\, E(\beta, V)\ , \quad (6)$$

where $\beta = 1/k_b T$. As starting point for the integration, we can take the classical, high temperature limit ($\beta_1 \to 0$) where the predictions from all nodal surfaces agree. From Fig. S1, we can conclude that our HF nodes are significantly better than FP and Pollock nodes.

Method	ρ (g cm^{-3})	ρ/ρ_0	$T(K)$	E (Ha/atom)	ϵ_E (Ha/atom)	P (GPa)	ϵ_P (GPa)
PIMC	2.329	1	129341301	9181.8930	3.6180	1335190.7	526.0
PIMC	2.329	1	64670651	4574.1180	3.4980	666626.4	507.1
PIMC	2.329	1	32335325	2265.3520	3.2550	331901.2	470.4
PIMC	2.329	1	16167663	1100.3200	1.8800	163533.0	271.7
PIMC	2.329	1	8083831	482.3270	1.4570	78489.3	203.0
PIMC	2.329	1	4041916	35.6380	1.0560	33636.6	151.5
PIMC	2.329	1	2020958	−128.4320	1.4580	14663.8	211.6
DFT-MD	2.329	1	750000	−247.1570	0.0008	3386.9	0.1
DFT-MD	2.329	1	505239	−266.9010	0.0006	1872.2	0.1
DFT-MD	2.329	1	250000	−282.8030	0.0005	691.0	0.4
PIMC	4.658	2	129341301	9171.0380	3.4810	2668660.3	1008.1
PIMC	4.658	2	64670651	4563.5600	3.3340	1331789.0	969.2
PIMC	4.658	2	32335325	2251.5260	3.3350	661773.8	965.2
PIMC	4.658	2	16167663	1080.9040	1.7860	324383.1	514.1
PIMC	4.658	2	8083831	439.5750	1.6430	152336.7	445.7
PIMC	4.658	2	4041916	12.3270	1.1950	65200.4	346.3
PIMC	4.658	2	2020958	−146.2080	1.3640	27553.5	396.8
DFT-MD	4.658	2	1010479	−231.9070	0.0030	10398.8	5.3
DFT-MD	4.658	2	750000	−252.4430	0.0030	6724.3	4.3
DFT-MD	4.658	2	505239	−269.6440	0.0040	3866.4	8.6
DFT-MD	4.658	2	250000	−283.2340	0.0060	1602.7	5.8
DFT-MD	4.658	2	100000	−287.4370	0.0080	629.7	4.1
DFT-MD	4.658	2	50000	−288.4070	0.0060	358.8	4.3
PIMC	6.987	3	129341301	9169.1970	3.1060	4003930.0	1348.8
PIMC	6.987	3	64670651	4547.5440	3.5220	1992509.2	1532.7
PIMC	6.987	3	32335325	2235.4160	3.2940	987707.6	1428.8
PIMC	6.987	3	16167663	1067.9070	2.2080	483879.2	956.5
PIMC	6.987	3	8083831	408.9970	1.9730	223935.3	835.2
PIMC	6.987	3	4041916	0.8250	1.5560	96497.2	677.6
PIMC	6.987	3	2020958	−159.5200	1.8080	38095.5	789.1
DFT-MD	6.987	3	1010479	−236.1540	0.0060	15607.2	27.4
DFT-MD	6.987	3	750000	−255.1520	0.0020	10228.1	21.0
DFT-MD	6.987	3	505239	−270.9450	0.0150	6020.6	27.0
DFT-MD	6.987	3	250000	−283.3580	0.0130	2653.2	7.8
DFT-MD	6.987	3	100000	−287.2920	0.0070	1237.0	5.8
DFT-MD	6.987	3	50000	−288.2310	0.0090	823.5	7.8
PIMC	9.316	4	129341301	9160.5960	3.4840	5335104.8	2020.1
PIMC	9.316	4	64670651	4551.1630	3.5780	2660714.0	2077.3

Continued on the following page.

Method	ρ (g cm^{-3})	ρ/ρ_0	$T(K)$	E (Ha/atom)	ϵ_E (Ha/atom)	P (GPa)	ϵ_P (GPa)
PIMC	9.316	4	32335325	2228.9250	3.4630	1315670.2	2006.9
PIMC	9.316	4	16167663	1059.1460	2.4510	644388.0	1408.0
PIMC	9.316	4	8083831	390.6560	1.7500	295039.8	953.0
PIMC	9.316	4	4041916	−9.0920	1.2470	126325.6	723.0
PIMC	9.316	4	2694610	-109.3620	1.6440	77593.7	954.1
PIMC	9.316	4	2020958	−162.7230	0.8820	51815.1	518.4
DFT-MD	9.316	4	2020958	−162.3860	0.0460	53994.0	49.3
DFT-MD	9.316	4	1010479	−238.9270	0.0090	21127.6	48.5
DFT-MD	9.316	4	750000	−256.8640	0.0140	14000.3	44.5
DFT-MD	9.316	4	505239	−271.6910	0.0090	8399.0	19.8
DFT-MD	9.316	4	250000	−283.3240	0.0080	3897.3	7.7
DFT-MD	9.316	4	100000	−287.0760	0.0100	2035.8	9.7
DFT-MD	9.316	4	50000	−287.9990	0.0060	1491.6	7.2
PIMC	11.645	5	129341301	9154.7710	1.6460	6666339.6	1194.9
PIMC	11.645	5	64670651	4536.3090	1.6700	3317133.6	1210.4
PIMC	11.645	5	32335325	2224.0050	1.6780	1643487.2	1214.9
PIMC	11.645	5	16167663	1047.8130	1.8210	800998.2	1306.9
PIMC	11.645	5	8083831	371.3900	1.6760	364447.7	1143.3
PIMC	11.645	5	4041916	−16.3540	1.3620	156361.8	993.2
DFT-MD	11.645	5	2020958	−166.7740	0.0710	67206.6	97.1
DFT-MD	11.645	5	1010479	−240.8560	0.0270	26892.2	107.7
DFT-MD	11.645	5	750000	−258.0590	0.0090	18026.4	43.7
DFT-MD	11.645	5	505239	−272.1630	0.0100	10955.4	23.8
DFT-MD	11.645	5	250000	−283.1680	0.0130	5363.5	12.8
DFT-MD	11.645	5	100000	−286.7950	0.0070	3078.9	7.0
DFT-MD	11.645	5	50000	−287.6990	0.0050	2420.6	6.6
PIMC	13.974	6	129341301	9144.6710	3.5480	7992810.7	3087.8
PIMC	13.974	6	64670651	4540.0170	3.3760	3986259.3	2943.9
PIMC	13.974	6	32335325	2220.7620	3.4170	1972368.7	2960.8
PIMC	13.974	6	16167663	1038.4910	2.4970	957890.7	2124.0
PIMC	13.974	6	8083831	361.2450	2.2060	435422.9	1865.3
PIMC	13.974	6	4041916	−17.6870	1.9410	190435.9	1688.3
PIMC	13.974	6	2020958	−164.5430	1.4990	81182.1	1308.2
DFT-MD	13.974	6	2020958	−169.9650	0.1390	80923.8	182.8
DFT-MD	13.974	6	1010479	−242.3660	0.0470	32508.1	136.8
DFT-MD	13.974	6	750000	−258.9620	0.0180	22007.2	80.1
DFT-MD	13.974	6	505239	−272.4350	0.0370	13834.1	93.4
DFT-MD	13.974	6	250000	−282.9850	0.0160	7014.2	18.5
PIMC	18.632	8	129341301	9137.0560	3.4650	10652592.7	4018.6
PIMC	18.632	8	64670651	4523.4160	3.3800	5300935.9	3908.0
PIMC	18.632	8	32335325	2205.0500	3.5490	2617832.7	4099.8
PIMC	18.632	8	16167663	1022.1250	1.9640	1268337.8	2234.7
PIMC	18.632	8	8083831	340.2690	1.8940	572026.0	2134.0
PIMC	18.632	8	4041916	−25.8850	1.3170	252032.9	1535.4
DFT-MD	18.632	8	2020958	−175.0180	0.0770	109041.1	174.0
DFT-MD	18.632	8	1010479	−244.5310	0.0180	44810.9	106.4
DFT-MD	18.632	8	750000	−260.0340	0.0490	31467.4	246.7
DFT-MD	18.632	8	505239	−272.7980	0.0060	19547.6	32.5
DFT-MD	18.632	8	250000	−282.4490	0.0080	11047.4	16.9

TABLE S1: Equation of state table for hot, dense silicon providing the internal energy, E, and pressure, P, as function of density, ρ, and temperature, T. ϵ denotes the statistical error bars. The zero of energy taken from a completely ionized system. $\rho_0 = 2.329$ g cm^{-3}.